An instrumented indentation technique for estimating fracture toughness of ductile materials: A critical indentation energy model based on continuum damage mechanics

Jung-Suk Lee [a,*], Jae-il Jang [b], Baik-Woo Lee [a], Yeol Choi [a,c],
Seung Gun Lee [a], Dongil Kwon [a]

[a] *School of Materials Science and Engineering, Seoul National University, Seoul 151-744, Republic of Korea*
[b] *Division of Materials Science and Engineering, Hanyang University, Seoul 133-791, Republic of Korea*
[c] *Frontics, Inc., Research Institute of Advanced Materials, Seoul National University, Seoul 151-744, Republic of Korea*

Abstract

We suggest a new instrumented indentation technique for estimating fracture toughness of ductile materials. This technique is based on two key concepts. First, the indentation energy to the characteristic fracture initiation point during indentation may be closely related to a material's resistance to fracture, i.e., fracture toughness. Second, the characteristic fracture initiation point can be determined by exploiting the basic concepts of continuum damage mechanics. To verify the applicability of the suggested technique, indentation tests and conventional fracture toughness tests were performed on four ductile materials. The estimated fracture toughness values obtained from the indentation technique showed good agreement (within approximately 10% error) with those from conventional fracture toughness tests.
© 2005 Acta Materialia Inc. Published by Elsevier Ltd. All rights reserved.

Keywords: Microindentation; Fracture; Toughness; Continuum damage mechanics

1. Introduction

Because fracture toughness, which indicates the resistance to crack growth, is very important in assessing structural integrity, many methods for measuring it are now detailed in many standards [1–3]. These standard methods generally require specific specimen geometry (typically, single-edge notched beam sample for three-point bending or compact-tension specimen for tensile loading) and size. In addition, the complex testing procedures (including fatigue precracking and crack length measurement) must be well controlled, thus making fracture toughness evaluation quite difficult. Above all, current fracture toughness testing methods cannot be directly applied to in-service industrial structures due to their destructive nature.

Because indentation techniques are relatively simple to perform, they have been suggested as a way to alleviate the drawbacks of current fracture toughness test methods. Lawn et al. [4,5], using a simple relationship between fracture toughness, radial crack length, and indentation load, showed that the fracture toughness of a brittle material could be measured by Vickers indentations. Recently, Byun et al. [6] proposed an indentation energy to fracture (IEF) model that relates indentation deformation energy to fracture energy in order to estimate fracture toughness from instrumented spherical indentation. However, these current indentation techniques can be applied only to brittle materials with low fracture toughness ($K_{IC} \leqslant 10$ MPa(m)$^{0.5}$) or lower shelf energy level in the ductile–brittle transition temperature region of ductile materials. Because indentation does not induce severe cracking in ductile materials, estimating fracture toughness in ductile materials by using indentation is an issue as yet unsolved.

---

* Corresponding author. Tel.: +82 2 880 8404; fax: +82 2 886 4847.
E-mail address: jslee119@plaza.snu.ac.kr (J.-S. Lee).

Here we suggest a new model for evaluating fracture toughness of ductile materials using a spherical indentation technique. Exploiting the finite element analysis observation that the stress triaxiality beneath the indenter is similar to that ahead of the crack tip in a conventional fracture toughness testing sample, we show that indentation deformation energy to a certain indentation depth (which is a characteristic fracture initiation point) can be correlated with energy required for fracture in ductile materials. The characteristic fracture initiation point was determined by using concepts from continuum damage mechanics (CDM). To verify the applicability of this new technique, fracture toughness values of four ductile structural steels were estimated and compared with those from a standard crack tip opening displacement (CTOD) test, one of the most popular standard methods for evaluating the fracture toughness of ductile materials [1–3].

2. Preliminary finite element simulation

In the cracked (or notched) specimens, a local constraint force characterizes the stress and strain fields around the crack tip (or notch root). The effects of constraint or stress state on fracture have been emphasized in many studies [7–11] since it has been found that fracture toughness decreases with increasing degree of constraint. One of the most popular ways to quantify the out-of-plane constraint effect is to evaluate the stress triaxiality, which is usually defined as the ratio of mean stress (σ_m) to the equivalent stress (σ_{eq}) [7,12]

$$t = \frac{\sigma_m}{\sigma_{eq}}, \tag{1}$$

where the mean stress and equivalent stress are defined, respectively, as

$$\sigma_m = \frac{\sigma_1 + \sigma_2 + \sigma_3}{3}, \tag{2}$$

$$\sigma_{eq} = \frac{1}{\sqrt{2}} \left[(\sigma_1 - \sigma_2)^2 + (\sigma_2 - \sigma_3)^2 + (\sigma_3 - \sigma_1)^2 \right]^{\frac{1}{2}}, \tag{3}$$

where σ_1, σ_2 and σ_3 are the principal stress components in the radial, circumferential and axial directions, respectively. To identify stress triaxialities of both crack tip and indenter tip, preliminary finite element simulations were performed using the commercial software ABAQUS.

Fig. 1 shows the geometry of a single-edge-cracked beam specimen for the CTOD test. In accordance with the ASTM testing recommendation [1], both the thickness-to-width (B/W) and crack length-to-width (a/W) ratios were fixed at 0.5; the width was 18 mm. Its finite element model has 2768 elements and 13,245 nodes with symmetry conditions fully utilized for efficient computation. To avoid problems associated with incompressibility, a reduced integration 20-node brick element (C3D20R element in ABAQUS) was used for 3D calculations. Twenty fans of elements surrounded the crack tip circumferentially, and 10 elements along the thickness direction
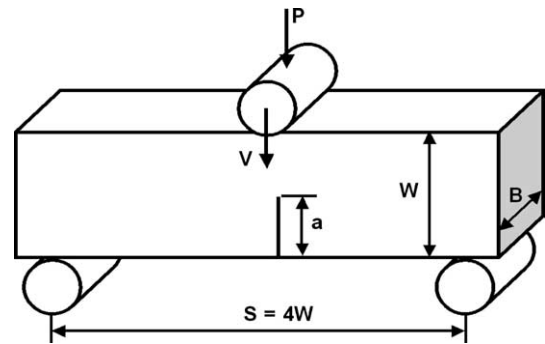

Fig. 1. Geometry of CTOD specimen used in this study.

were designed to resolve the stress gradient along the thickness direction. The finite element simulation for the CTOD test was set up under displacement-controlled conditions; the maximum load was applied to reach the displacement corresponding to the critical CTOD value (δ_{IC}) of the specimen.

The indentation response was simulated by an axisymmetric 2D model that can fully describe the indentation response without the many meshes and complex calculations of a 3D model. A spherical indenter of 500 μm diameter, 0.07 Poisson's ratio and 600 GPa elastic modulus was modeled. A total of 2411 four-node bilinear axisymmetric elements were used for the indented solid. The mesh was well tested for convergence and was determined to be insensitive to far-field boundary conditions. Finite element simulation for the indentation test was also set up under displacement-controlled conditions, with loading to indentation depth 150 μm and then unloading. The material used was API X70 steel, whose yield strength, tensile strength, Young's modulus, and work-hardening exponent are 597 MPa, 789 MPa, 213 GPa, and 0.128, respectively.

The maximum stress triaxialities (t_{max}) ahead of the crack tip could be calculated based on the finite element simulation results for the CTOD test. Fig. 2(a) shows the change in t_{max} along the displacements V in the loading axis; V_{max} is the maximum displacement of the upper jig, i.e., the displacement corresponding to fracture toughness (δ_{IC}). Through monomolecular growth fitting (see Fig. 2(a)), it is shown that the triaxiality is about the value of 2.3 at initial loading, and then nearly converges to about 3.0 as the load increases.

Fig. 2(b) shows the change in maximum stress triaxiality (t_{max}) beneath the indenter, based on the finite element simulation result. As the indentation depth h increases, triaxiality increases gradually and converges to about 3.2. As in the crack tip case, monomolecular growth fitting between the triaxiality and the ratio of indentation depth to indenter radius (h/R) works excellently, showing that the value of triaxiality is about 2.1 at initial loading and then converges gradually to about 3.2 as the indentation load increases.

It is interesting that the change in triaxiality beneath the indenter is very similar to that ahead of the crack tip, i.e., that the stress triaxialities in both cases are in the range
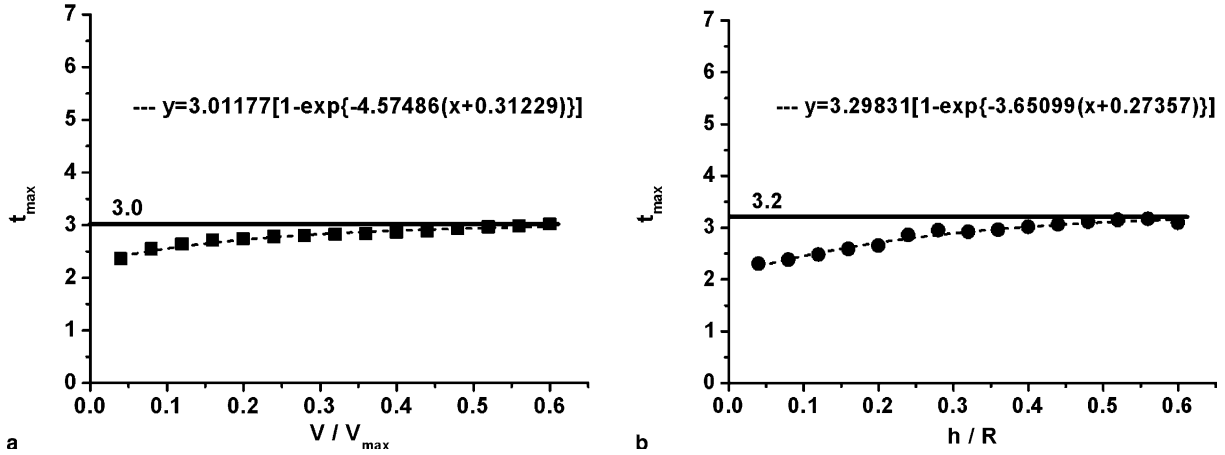
Fig. 2. Change in stress triaxiality with increasing deformation: (a) crack tip and (b) indenter tip.

2.1–2.2 at initial loading and then converge to 3.0–3.2. This observation suggests that the indentation deformation energy per unit area absorbed to critical indentation depth may be similar to the fracture energy required for fracture initiation.

3. Theoretical model

3.1. Critical indentation energy model

For a crack of length $2a$ in an infinite plate, the fracture toughness is given by [13]:

$$K_{JC} = \sigma_f \sqrt{\pi a}, \tag{4}$$

where σ_f is the remote tensile stress at fracture. According to Griffith theory, σ_f is given by [13]:

$$\sigma_f = \sqrt{\frac{2E w_f}{\pi a}}, \tag{5}$$

where E is the elastic modulus and w_f is energy per unit area required to create a crack surface (or the deformation region ahead of crack tip). Combining Eqs. (4) and (5), the relationship between w_f and K_{JC} becomes

$$K_{JC} = \sqrt{2E w_f}. \tag{6}$$

Although Eqs. (4) and (5) apply only to a through crack in an infinite plate, Irwin [14] has proved that Eq. (6) is a general relationship that can be applied to all configurations.

To estimate K_{JC} via the indentation technique, w_f must be determined using only indentation parameters. We can confirm from preliminary finite element simulation that the triaxiality ahead of the indenter tip is in the range 2–3 and that the degree of constraint in the deformed indentation region is similar to that ahead of the crack tip. Hence the indentation energy per unit contact area can be related to w_f if there exists a characteristic fracture initiation point during the indentation process. This energy, henceforth called the critical indentation energy, is calculated from the indentation load–depth curve as follows:

$$2w_f = \lim_{h \to h^*} \int_0^h \frac{4L}{\pi d^2} \, dh, \tag{7}$$

where L is the applied indentation load, h the indentation depth, d the hardness impression diameter, and h^* the critical indentation depth corresponding to the characteristic fracture initiation point. The term on the left ($2w_f$) is the energy for the formation of two crack surfaces. The following section describes the determination of h^* in detail.

3.2. Determination of h^*

Since there is no distinguishable mark to identify fracture during indentation, h^* in Eq. (7) cannot be measured by direct methods such as optical microscopy or scanning electron microscopy (SEM). Thus, to determine h^* indirectly, we adopted concepts of CDM, which has been widely used to predict failure in structures loaded statically and dynamically. The seminal idea for this mechanics is due to Kachanov [15], who introduced the damage variable D defined in Eq. (8) and related to the surface density of microdefects in the material:

$$D = \frac{s_D}{s}, \tag{8}$$

where s and s_D are, respectively, the cross-sectional area of the loaded region and the reduced area due to microdefects. In Eq. (8), D can be also represented by an elastic modulus change using Lemaitre's strain-equivalence principle [16]

$$D = 1 - \frac{E_D}{E} \quad \text{or} \quad E_D = E(1 - D), \tag{9}$$

where E_D and E are the elastic modulus of the damaged and undamaged material, respectively. Thus, E_D decreases as the degree of damage in the material increases.

If we assume that possible damage (such as voids nucleated in ductile material) beneath the indenter increases with increasing indentation depth, E_D can also decrease during indentation. In this case, E_D is represented with indentation parameters [17]:

$$E_D = \frac{1-v^2}{\left(\frac{1}{E_r} - \frac{1-v_i^2}{E_i}\right)} = \frac{1-v^2}{\left(\frac{2\sqrt{A_C}}{\sqrt{\pi}S} - \frac{1-v_i^2}{E_i}\right)}, \qquad (10)$$

where v and v_i are the Poisson's ratios of the material and indenter, respectively. Note that v is not affected by damage accumulation [15,16]. E_r is the reduced modulus, E_i is the elastic modulus of the indenter, A_C is the contact area between indenter and material, and S is the unloading slope. The values of E_D at various indentation depths can be calculated at each unloading. Fig. 3 shows an example of E_D with h obtained from indentation. (We discuss this decrease in E_D with h in more detail in Section 5.1 below.) If a critical value of the damaged material elastic modulus (E_D^*), which is the damaged material elastic modulus at fracture initiation, can be determined in Fig. 3, one can obtain h^*, i.e., the indentation depth at the fracture initiation point.

The value of E_D^* can be determined from the critical damage value (D^*) through Eq. (9). The material beneath the indenter experiences localized shear stresses due to compressive indentation force in the loading axis. If the shear stresses induce void nucleation, the void volume fraction (f) may increase with increasing spherical indentation load [18–20]. As the void volume fraction increases, s_D and thus D in Eq. (8) increase. By assuming that voids are uniformly distributed with nearest-neighbor spacing l, f and D can be calculated using the void radius (r). For a cross-sectional area of one void πr^2 per total area l^2, D can be described as $\pi r^2 / l^2$, while for void volume $4\pi r^3 / 3$ per total volume l^3, f can be given as $(4\pi r^3/3)/l^3$. By combining these equations, D can be represented in terms of f as

$$D = \frac{\pi}{\left(\frac{4}{3}\pi\right)^{\frac{2}{3}}} f^{\frac{2}{3}} \quad \text{or} \quad f = \frac{\frac{4}{3}\pi}{\pi^{\frac{3}{2}}} D^{\frac{3}{2}}. \qquad (11)$$

Thus, the critical damage value (D^*) can be determined if we know the critical void volume fraction (f^*), which means the value of f at the fracture initiation point. Numerical analyses by Andersson [21] show $f^* \cong 0.25$ at the initi-
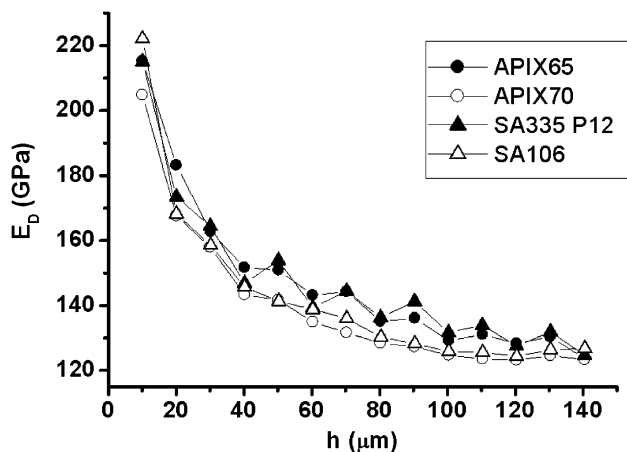
ation of stable crack growth in ductile materials, and Tvergaard and Needleman [22] has described the process of stable crack growth from a modified Gurson model [23] using this criterion. From these results, the value $f^* = 0.25$ may be employed here to determine the critical value of the damaged material elastic modulus of a ductile material, and thus its fracture initiation point during indentation. (The validity of this $f^* = 0.25$ is re-evaluated through interrupted tensile testing in Section 5.2.) Therefore, one may determine the critical damage variable D^* simply by putting the value of f^* into Eq. (11); then the value of E_D^* can then be calculated from Eq. (9). Finally, h^* (required for calculating Eq. (7)) can be obtained as the depth corresponding to the critical damaged material elastic modulus E_D^*.

4. Experimental details

To verify the applicability of this new model, the instrumented indentation tests were carried out on four commercial-grade ductile materials, API X65, X70, ASME SA335 P12 and SA106 (these are widely used as structural steels; their chemical compositions and mechanical properties are listed in Table 1), using an AIS 3000R (Frontics, Inc., Seoul, Korea) whose load and depth resolution are 0.02 N and 0.10 μm, respectively. The maximum indentation depth was 150 μm and multiple loading–unloading cycles were applied at 10 μm intervals using a 500 μm-diameter ball indenter with $v_i = 0.07$ and $E_i = 600$ GPa. Both loading and unloading rates were fixed at 0.1 mm/min. At least five sets of indentation data were obtained from indentation tests for each material, and the average value was used in analyzing the fracture toughness. In addition, after indentation testing, cross-sections beneath the indenter tip were observed by SEM to verify damage accumulation by voids. The cross-sections were obtained by cutting along the center of the indenter impression.

For comparison, CTOD tests were performed on the same materials according to ASTM E1290 [1]. The geometry and size of the specimen are the same as that used in the preliminary finite element simulation. At least five tests were done for each material, and the average value was used as the representative fracture toughness.

In addition, interrupted tensile tests were done to obtain the critical void volume fraction and critical elastic modulus. Direct measurement of the void volume fraction in the mechanically tested specimen is very difficult, since in neither void observation nor calculation of the area occupied by voids can the researcher's subjective judgment be excluded. Hence, we performed interrupted tensile tests, and then each elastic modulus from unloading curves was converted into void volume fraction. In particular, the void volume fraction obtained from the elastic modulus of the unloading curve at the onset of fracture in tensile specimens is compared with the critical void volume fraction proposed by Andersson [21] and Tvergaard and Needleman [22].

Fig. 3. Change in damaged material elastic modulus with indentation depth.

Table 1
Chemical compositions and mechanical properties of ductile materials

Materials	Components (wt.%)												
	C	P	Mn	S	Si	Mo	Cr	Cu	Ti	Nb	V	Ni	Fe
API X65	0.08	0.019	1.45	0.003	0.31	–	–	–	–	–	–	–	Bal.
API X70	0.04	0.016	1.76	0.001	0.281	0.194	0.058	0.193	0.023	0.067	0.001	–	Bal.
ASME SA335 P12	0.08	0.01	0.45	0.01	0.31	0.55	1.15	–	–	–	–	–	Bal.
ASME SA106	0.35	0.009	1.06	0.025	0.10	0.03	0.40	0.13	–	–	0.004	0.11	Bal.

	Properties					
	YS (MPa) (true stress)	UTS (MPa) (true stress)	n	K (MPa)	E (GPa)	δ_{IC} (mm) (obtained in this work)
API X65	441	623	0.169	868	210	0.54 ± 0.08
API X70	597	789	0.128	1056	213	0.66 ± 0.11
ASME SA335 P12	290	565	0.236	882	194	1.30 ± 0.14
ASME SA106	328	653	0.221	979	209	0.63 ± 0.08

5. Results and discussions

5.1. Change in elastic modulus

The change in damaged material elastic modulus E_D with increasing indentation depth h was calculated from the indentation unloading curves according to Eq. (10). Contact stiffness was calculated by the Oliver–Pharr method [17], while the contact area A_C was determined by considering the pile-up behavior around the indenter using Matthews' method [24]. Fig. 3 shows the results for all materials used here. It is clear that E_D decreases with increasing depth. To confirm the damage accumulation during indentation, the region below the indentation was observed by SEM. Some sample observations are shown in Fig. 4. We see that (1) there are in fact voids beneath the indenter and (2) the void volume fraction increases with increased depth. The images in the figure show situations in which the indentation load did not reach the damage threshold force (Fig. 4(a)), cavity dislocations or voids initially nucleated (Fig. 4(b)), voids grew (Fig. 4(c)), and a microcrack advanced to approximately 10 μm (Fig. 4(d)). The initial void orientation is not orthogonal with respect to the indentation-loading axis but is inclined to it at about 45°. As the applied load increases, two wings emerged from the upper and lower parts of the void and grew parallel to the loading axis.

Void formation even under compressive forces can be explained by the dislocation pile-up model and angled crack growth mechanism proposed by Zener [25] and Dyskin et al. [26], respectively. During spherical indentation, the localized shear stresses beneath the indenter increase with indentation load and enable dislocations to slip. On slipping, dislocations frequently pile up on slip planes at obstacles such as grain boundaries, second phases, or sessile dislocations. The leading dislocation in the pile-up is acted on not only by the applied shear stress but also by interaction forces from the other dislocations in the pile-ups, leading to a high stress concentration in the pile-up. When many dislocations are contained in the pile-up, the stress on the dislocation at the head of a pile-up can approach the theoretical shear stress of material. At this critical stress value, the dislocations at the head of the pile-up are pushed so close together that they coalesce into a wedge crack or cavity dislocation. Since the wedge crack or cavity dislocation does not propagate immediately in ductile metal, it can be regarded as a void.

As deformation beneath the indenter progresses, the size and numbers of voids increase and the spacing between them becomes smaller. Closer spacing causes voids to interconnect, and interconnecting voids enable a very small microcrack of length only 1–2 μm to form (Fig. 4(c)). Since a microcrack due to shear stress is inclined to the compressive indentation-loading axis at approximately 45°, the tip of the microcrack experiences tensile stress perpendicular to the loading axis. The concentration of tensile stress at the microcrack tip makes the microcrack grow. In addition, microcrack growth progresses in the direction perpendicular to the concentrated tensile stress, showing maximum stress intensity factor. The growing microcrack has two symmetric (i.e., left and right wing) surfaces that are equally favored for shear strain concentration at the tip.

5.2. Critical void volume fraction

We now return to the issue of $f^* = 0.25$ as proposed by Andersson [21] and Tvergaard and Needleman [22]. This condition is very important simply because E_D^* (and thus h^*) can be calculated by substituting $f = f^*$ in Eqs. (9)–(11). To verify the value of the critical void volume fraction, interrupted tensile tests were carried out on all the ductile materials used in this study; the stress–strain curves obtained are shown in Fig. 5. The unloading and reloading paths seem to overlap exactly for each interruption, but increasing the magnification of the figure, as in Fig. 6, reveals clear hysteresis loops. Lemaitre and Chaboche [27] and Bonora et al. [28] suggest that elastic modulus should be measured from the unloading curve, because the elastic modulus from the reloading curve may be underestimated due to back-stress relaxation [29]. In addition, to exclude the nonlinear region of the unloading curve due to
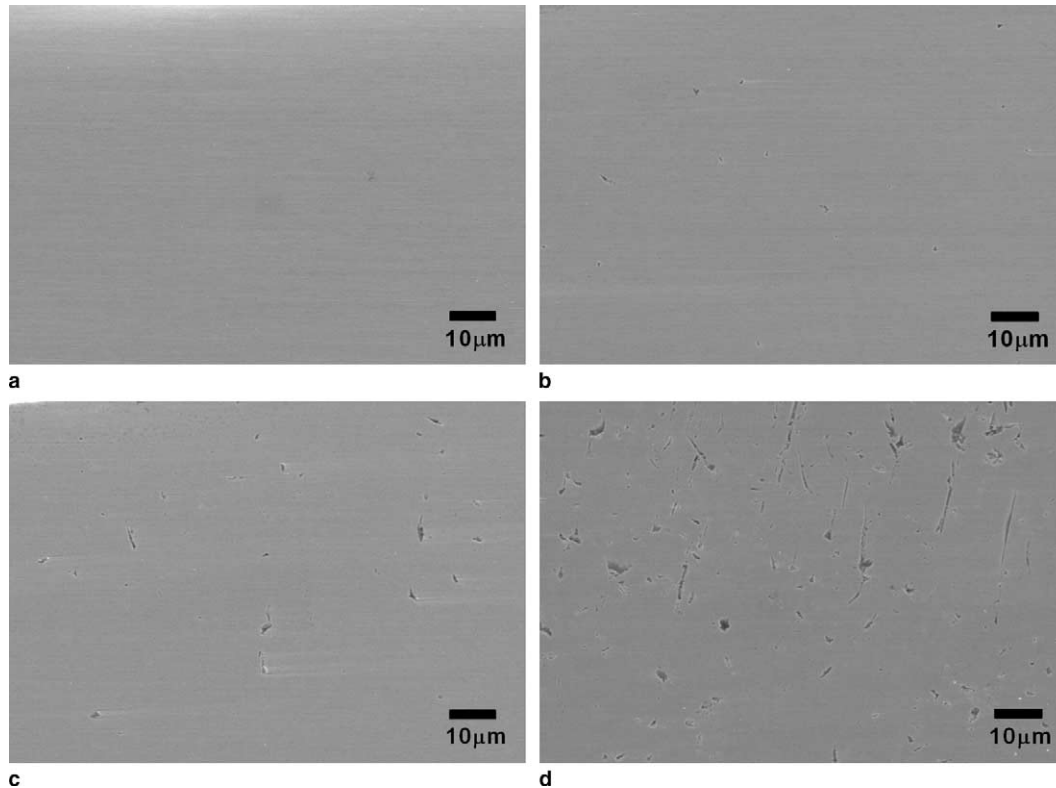
Fig. 4. Cross-sectional SEM images of API X65 below indentation after (a) 10 μm, (b) 30 μm, (c) 70 μm and (d) 140 μm indentation.
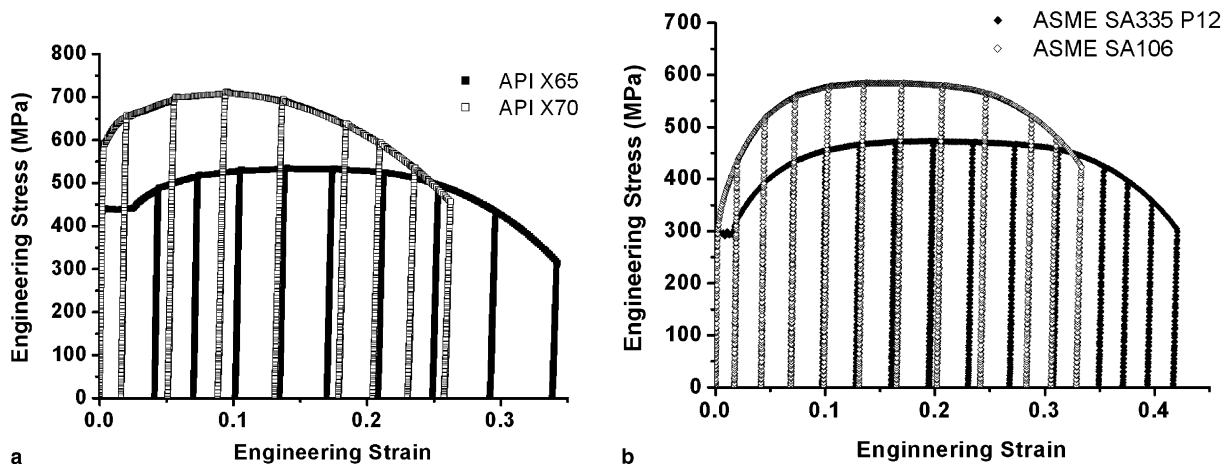

Fig. 5. Interrupted tensile curves of (a) API X65 and X70, and (b) SA335 P12 and SA106.

the back-stress relaxation or unloading delay time from machine sensitivity, only the linear region was fitted after eliminating its lower and upper 20%.

Damaged elastic moduli obtained from the interrupted tensile tests were converted to damage variable D using Eqs. (9)–(11). Fig. 7(a) and (b) show the changes in the damaged material elastic modulus and damage variable with the maximum principal engineering strain (e_I): as e_I increases, E_D decreases while D increases. This damage accumulation with increasing strain can be described by the following equation, derived by Bonora [30] based on a kinetic law of damage evolution for ductile materials [15,16]:

$$D = D_0 + (D_{cr} - D_0)\left\{1 - \left[1 - \frac{\ln(\varepsilon/\varepsilon_{th})}{\ln(\varepsilon_{cr}/\varepsilon_{th})}\right]^{\alpha}\right\}, \quad (12)$$

where α is a damage exponent characteristic of the material, D_0 the initial damage and D_{cr} damage at failure, and ε, ε_{th} and ε_{cr} are the applied strain, damage threshold strain and strain at failure, respectively.

The damage evolution law in Eq. (12) is characterized by a large number of small voids that nucleate around the included particles when the threshold strain is reached. When the strain increases, the existing void dimension remains almost constant while more new voids
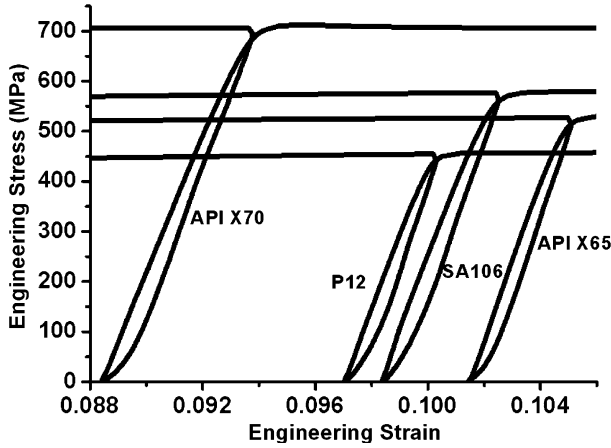
Fig. 6. Enlarged curves from interrupted tensile tests.

are nucleated. In the loaded region of the material, damage accumulates rapidly with the increasing strain because of the formation of very large numbers of microvoids. Once this process is saturated, with consequent reduction of void spacing, increasing strain results in the sudden coalescence of voids and failure of the material. In Eq. (12), D_{cr} is the value calculated by substituting the elastic

modulus obtained from unloading data at fracture on the interrupted tensile curve into Eq. (9), and is the same as D^*. The true strain ε can be replaced by $\ln(1 + e_I)$, using the relationship between the true strain and the engineering strain. If the bond between the matrix and the particle is weak, ε_{th} can be of the same order of magnitude as the matrix elastic strain at the proportional limit, and exact determination is difficult. But if extensive plastic flow occurs prior to damage, ε_{th} can be identified accurately [30,31]. Since damage accumulates soon after yielding in the present work, ε_{th} can be approximated as the yield strain of each material. Assuming that the virgin material has no damage, D_0 is equal to zero. Using data obtained from the interrupted tensile test, we obtain the value of α by fitting $\ln(D_{cr} - D_0)$ vs. $\ln[\ln(\varepsilon_{cr}/\varepsilon_{th})]$ in the following equation of Bonora [30]:

$$(D_{cr} - D_0)^{1/\alpha} = \frac{1}{\alpha} \frac{K^2}{2ES_0} \ln\left(\frac{\varepsilon_{cr}}{\varepsilon_{th}}\right),\tag{13}$$

where K is the strength coefficient and S_0 is a material constant.

In addition to the damage variable–strain relationship experimentally measured by interrupted tensile tests, the relations calculated with Eqs. (12) and (13) are also
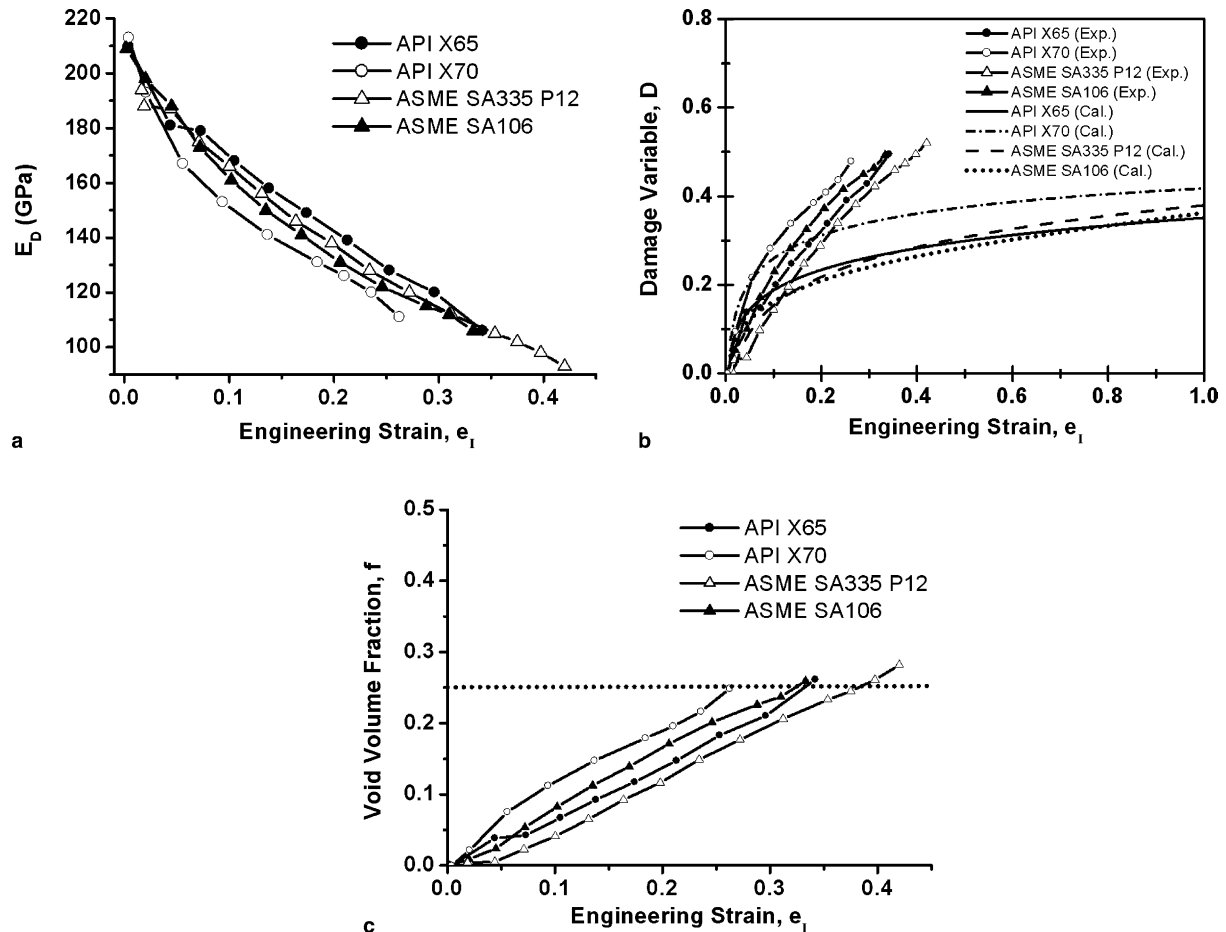

Fig. 7. Changes in (a) damaged elastic modulus, (b) damage variable and (c) void volume fraction with increasing strain.

shown in Fig. 7(b). The calculated results are in good agreement with experimental results for the low-strain regime (i.e., damage initially increases rapidly). After some strain, however, the experimental damage values are much higher than those theoretically calculated according to the damage evolution law (Eqs. (12) and (13)).

This difference between the theoretical value of damage and the experimental value can be explained by the stress triaxiality due to the necking behavior. Eq. (12) was derived simply by assuming uniaxial tensile loading. However, when plastic strain reaches uniform elongation or tensile load reaches maximum load, necking generally occurs. The formation of a neck introduces a complex triaxial state of stress since the neck plays the role of a mild notch. Hence, taking into account this triaxial state of stress, Eq. (12) should be modified as [30]:

$$D = D_0 + (D_{cr} - D_0)\left\{1 - \left[1 - \frac{\ln(p/p_{th})}{\ln(\varepsilon_{cr}/\varepsilon_{th})}f\left(\frac{\sigma_m}{\sigma_{eq}}\right)\right]^\alpha\right\} \quad \text{and}$$

$$f\left(\frac{\sigma_m}{\sigma_{eq}}\right) = \frac{2}{3}(1+v) + 3(1-2v)\left(\frac{\sigma_m}{\sigma_{eq}}\right)^2, \tag{14}$$

where p is accumulated plastic strain and p_{th} is accumulated plastic strain at the damage threshold. Since many studies [30–32] have confirmed the validity of Eq. (14), one might expect that the stress triaxiality correction can considerably reduce the difference between experimental and calculated results in Fig. 7(b).

Fig. 7(c) shows the change in void volume fraction (as converted from experimental values of the damage variable in Fig. 7(b) through Eq. (11)) with increasing strain. It is seen that, as expected from Eq. (11), the fraction increases as strain increases. It is noteworthy that, although the patterns of increase in volume fraction were somewhat different, the values of f at fracture became around 0.25–0.27 for all the materials. This means that the void volume fraction required to reach the fracture strain may be similar for all ductile materials, and that value is about 0.25, as previous studies proposed [21,22].

5.3. Verification

To assess the validity of our indentation technique for estimating fracture toughness of ductile materials, fracture toughness values estimated by the indentation tests were compared with those from CTOD tests.

Here we show how to determine h^* (needed for calculating Eq. (7)) for API X70 steel, one of the ductile materials used in this work. Since $f^* = 0.25$ has been shown to be a reasonable condition for ductile fracture initiation, D^* can be determined as 0.48 by putting $f^* = 0.25$ into Eq. (11). The almost undamaged material elastic modulus (which can be obtained from the first point in Fig. 3) of this material is about 204 GPa. Although even the first point might include damage, this 204 GPa is very close to the undamaged value (213 GPa) obtained from tensile tests.

By Eq. (9), therefore, the elastic modulus corresponding to D^*, i.e., E_D^*, becomes 106 GPa ($= 204 \times (1 - 0.48)$). Note that, for a ductile material such as X70, the critical indentation depth h^* corresponding to this E_D^* cannot be obtained directly from indentation tests (such as in Fig. 3), and hence must be determined by extrapolation of the proper fit of E_D–h relations. Fig. 8 shows the relation of $\ln h$ and $\ln E_D$ for X70 steel, whose fitting line shows good linearity; the correlation factor of this fitting line (R) is more than 0.98. From extrapolation of the $\ln h$–$\ln E_D$ fitting curve, the value of $\ln h^*$ corresponding to $\ln E_D^*$ ($\ln 106$ (=4.67)) was determined as shown in Fig. 8. Finally, we can estimate K_{JC} values for all ductile materials used in the present work through Eqs. (6) and (7) by using h^* values determined in the same manner for each material.

Fig. 9 compares the fracture toughness K_{JC} obtained from the indentation technique and from conventional CTOD tests. To convert from CTOD values to K_{JC}, the following general equation was applied:
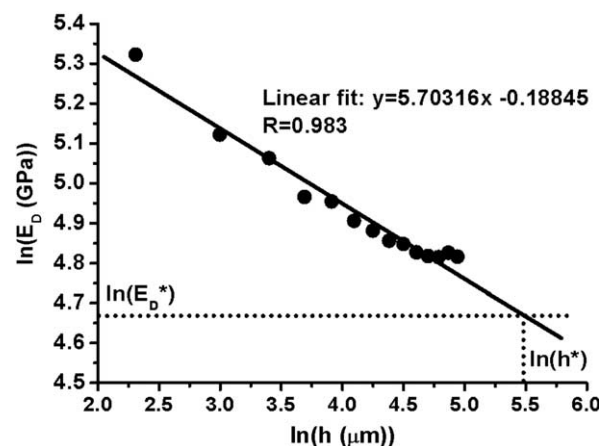

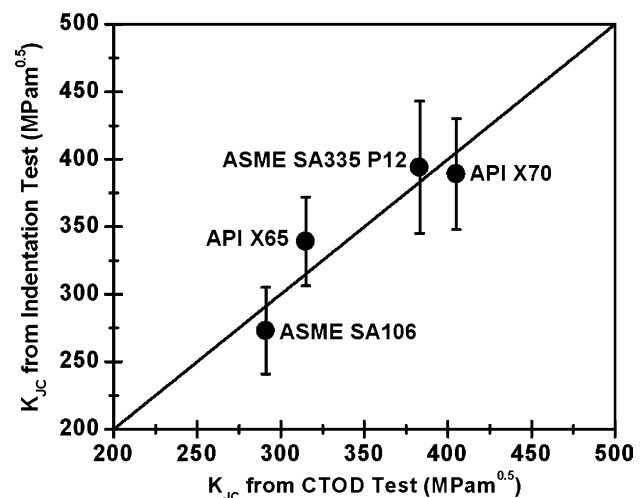Fig. 8. Relation between $\ln h$ and $\ln E_D$ for API X70.

Fig. 9. Comparison of fracture toughness in CTOD tests and indentation tests.

$$K_{\mathrm{JC}} = \sqrt{2\sigma_{\mathrm{Y}} E \delta_{\mathrm{IC}}}, \tag{15}$$

where σ_{Y} is the yield strength and δ_{IC} is the critical CTOD value. In the figure, the mean value and standard deviation of K_{JC} from the model are indicated while mean values of K_{JC} from CTOD tests are seen. The K_{JC} from indentation tests have about 10% self-standard deviation, and there is approximately 10% difference in the values between the indentation tests and CTOD tests. However, if we take into account that K_{JC} values from CTOD tests include a standard deviation of more than 10% (see Table 1; this deviation may arise because CTOD test is very sensitive to the location of precrack tip), Fig. 9 shows good agreement in K_{JC} values between the indentation tests and CTOD tests.

The above results for ductile materials support the validity of the new indentation technique suggested here, and it is expected that this technique can be applied to in situ estimation of the fracture toughness of ductile structural steels in a nondestructive way.

6. Conclusions

We propose a new instrumented indentation technique for estimating fracture toughness of ductile materials, the critical indentation energy model. It was shown that the fracture energy in Griffith theory can be correlated with the indentation energy to a characteristic fracture initiation point based on the finite element simulation results (which revealed that the degree of constraint ahead of indenter tip is similar to that ahead of crack tip). The concept of critical void volume fraction from continuum damage mechanics (CDM) was introduced to determine a characteristic point of fracture initiation during indentation. To verify this technique, the fracture toughness of four ductile materials was evaluated by both indentation and CTOD tests. The experimental results show good agreement in K_{JC} values between indentation and CTOD tests, boding well for future practical use of this technique.

References

[1] ASTM Standard E1290, Standard test method for plane-strain fracture toughness of metallic materials, 1993.
[2] ASTM Standard E1820, Standard test method for measurement of fracture toughness, 1996.
[3] BS7448, Fracture mechanics toughness test, The British Standards Institution, 1979.
[4] Lawn BR, Fuller ER. J Mater Sci 1975;10:2016.
[5] Lawn BR, Evans AG, Marshall DB. J Am Ceram Soc 1980;63:574.
[6] Byun TS, Kim SH, Lee BS, Kim IS, Hong JH. J Nucl Mater 2000;277:263.
[7] Mackenzie AC, Hancock JW, Brown DK. Eng Fract Mech 1977;9:167.
[8] Chen JH, Ma H, Wang GZ. Metall Trans A 1990;21:313.
[9] Wanlin G. Eng Fract Mech 1995;51:51.
[10] Ma H. Int J Fract 1998;89:143.
[11] Wang GZ, Chen JH. Metall Trans A 1996;27:1909.
[12] Mirza MS. J Mater Sci 1996;31:453.
[13] Griffith AA. Philos Trans A 1920;221:163.
[14] Irwin GR. J Appl Mech 1957;24:361.
[15] Kachanov L. Ivz Akad Nauk USSR Otd Tech 1958;8:26.
[16] Lemaitre J. J Eng Mater Tech 1985;107:83.
[17] Oliver WC, Pharr GM. J Mater Res 2004;19:3.
[18] Li H, Cai X, Cheng Q. Scripta Mater 2001;45:1381.
[19] Fougere GE, Riester L, Ferber M, Weertman JR, Siegel RW. Mater Sci Eng A 1995;204:1.
[20] Yang M, Akiyama Y, Sasaki T. J Mater Process Technol 2004;151:232.
[21] Andersson H. J Mech Phys Solid 1977;25:217.
[22] Tvergaad V, Needleman A. Acta Metall 1984;32:157.
[23] Gurson AL. J Eng Mater 1977;99:2.
[24] Matthews JR. Acta Metall 1980;28:311.
[25] Zener C. Fracturing of metals. Cleveland, OH: American Society of Metals; 1948. p. 3–31.
[26] Dyskin AV, Sahouryeh E, Jewell RJ, Joer H, Ustinov KB. Eng Fract Mech 2003;70:2115.
[27] Lemaitre J, Chaboche JL. Mechanics of solids materials. Cambridge: Cambridge University Press; 1990.
[28] Bonora N, Gentile D, Pirondi A, Newaz G. Int J Plast 2005;21:981.
[29] Sritharan T, Chandel RS. Acta Metall 1996;45:3155.
[30] Bonora N. Eng Fract Mech 1997;58:11.
[31] Chow CL, Wang J. Eng Fract Mech 1987;27:547.
[32] Le Roy G, Embury JD, Edward G, Ashby MF. Acta Metall 1981;29:1509.